A 10 nN resolution thrust-stand for micro-propulsion devices

Subha Chakraborty, Daniel G. Courtney, and Herbert Shea

EPFL

The following article appeared in: Review of Scientific Instruments (Vol.86, Issue 11, p. 115109) and may be found at http://dx.doi.org/10.1063/1.4935471 or at:
http://scitation.aip.org/content/aip/journal/rsi/86/11/10.1063/1.4935471

REVIEW OF SCIENTIFIC INSTRUMENTS 86, 115109 (2015)

A 10 nN resolution thrust-stand for micro-propulsion devices

Subha Chakraborty, Daniel G. Courtney, and Herbert Shea[a)]
Microsystems for Space Technologies Laboratory (LMTS), Ecole Polytechnique Federale de Lausanne (EPFL), Neuchatel, Switzerland

(Received 16 September 2015; accepted 26 October 2015; published online 16 November 2015)

We report on the development of a nano-Newton thrust-stand that can measure up to 100 μN thrust from different types of microthrusters with 10 nN resolution. The compact thrust-stand measures the impingement force of the particles emitted from a microthruster onto a suspended plate of size 45 mm $\times$ 45 mm and with a natural frequency over 50 Hz. Using a homodyne (lock-in) readout provides strong immunity to facility vibrations, which historically has been a major challenge for nano-Newton thrust-stands. A cold-gas thruster generating up to 50 μN thrust in air was first used to validate the thrust-stand. Better than 10 nN resolution and a minimum detectable thrust of 10 nN were achieved. Thrust from a miniature electrospray propulsion system generating up to 3 μN of thrust was measured with our thrust-stand in vacuum, and the thrust was compared with that computed from beam diagnostics, obtaining agreement within 50 nN to 150 nN. The 10 nN resolution obtained from this thrust-stand matches that from state-of-the-art nano-Newton thrust-stands, which measure thrust directly from the thruster by mounting it on a moving arm (but whose natural frequency is well below 1 Hz). The thrust-stand is the first of its kind to demonstrate less than 3 μN resolution by measuring the impingement force, making it capable of measuring thrust from different types of microthrusters, with the potential of easy upscaling for thrust measurement at much higher levels, simply by replacing the force sensor with other force sensors. [http://dx.doi.org/10.1063/1.4935471]

I. INTRODUCTION

Interest in microthrusters has grown significantly in the last two decades for possible applications in small satellites and for deep-space missions.[1,2] Several miniature thruster technologies, such as, cold-gas thrusters,[1,3] electrospray propulsion using liquid metals[4] or ionic liquids,[5–11] micro resisojets,[12,13] and micro pulsed plasma thrusters[13] are under investigation as prospective candidates targeting stable thrusts in the range of a few μN to several hundred μN. Several thrust-stands have been reported over the last few years for measuring thrust from these microthrusters with sub-μN resolutions.[14–24] Most of these thrust-stands operate by mounting the microthruster and a counter-mass on a pivoted torsion arm and measuring deflection under applied thrust with a displacement sensor, such as a capacitive sensor,[18] a laser displacement sensor (LDS),[19] a linear voltage differential transformer (LVDT),[20] or an optical interferrometer.[21] The natural frequencies of the reported thrust-stands are typically in the sub-Hz ranges and an additional damping mechanism, such as viscous damping,[20,22] damping coil,[17] electrostatic damping,[19] or Eddy current damping,[23] is used to reach steady deflection of the arms more quickly, and to minimize coupling to low-frequency facility vibrations, which is a major source of noise for thrust-stands with low natural frequencies. Different types of calibration sources are used for accuracy and resolution estimation and several of the thrust-stands have reported sub-100 nN resolution,[16,18,20–22] and as low as 10 nN.[19,23] The main challenges for such thrust-stands are facility vibrations, drift, effects of electrical and fluidic connectors to the thrusters, and the difficulty in operating with microthrusters with different thrust to mass ratios.

Another class of thrust-stand operates by firing the thruster at a target plate and measuring the force on the plate.[25–31] The present work describes one such thrust-stand. The method allows for easier adaptation to different types of thrusters by completely separating the thruster from the thrust measuring unit; thereby, removing sensitivity to the thruster mass and interconnects used for control or propellant supply. The best thrust resolution reported with this technique is 3 μN using an optical sensor.[27] However, the recorded force is not a direct measurement of thrust and measurements are complicated by unknown coefficients of restitution amongst impacting particles. Accordingly, a prior knowledge of the relation between the impingement force on the plate and the thrust on the thruster is required to determine thrust from the measured impingement force. This requirement also complicates the applicability of direct (e.g., mechanical or electrostatic) force based calibrations. Wu *et al.*[26] measured the impingement force from a nitrogen cold-gas thruster at atmospheric and lower pressure and found it to be within a few percent of computed thrust. Grubišić and Gabriel[27] reported a similar method and they obtained the similar relation between the computed thrust and measured impingement force from cold xenon and argon emission. Longmier *et al.*[29] measured thrust from a 5 kW xenon Hall Effect thruster and the results agree within a few percent from that measured directly with an inverted pendulum thrust-stand. The impingement force can be measured with different

a)Email: herbert.shea@epfl.ch

techniques, such as pressure tap,[26] optical displacement sensor,[27] or strain guage.[29] To date, this technique has been used for thrust measurement in the range of several mN or even higher.

In this article, we report on an impingement type thrust-stand with a thrust range of 100 μN with better than 10 nN resolution up to around 30 μN total thrust and better than 20 nN resolution above 30 μN. The thrust-stand measures the impingement force on a conductive low-mass plate using a commercially sourced micro-machined capacitive force sensor and is suitable for measuring thrust from many different types of microthrusters operating in the μN ranges. Compared with existing implementations,[26,27] the presented approach primarily differs in its use of a homodyne detection scheme. Here, the impinging beam is interrupted, by means dependent on the plume type, at a defined frequency f_{ref} which is greater than low-frequency facility vibrations yet below the natural frequency of the target plate. Accordingly, the natural frequency of the device is designed to be >50 Hz, compared with the few Hz or less typical of both existing impingement based stands[27] and direct-thrust torsional balances.[19,23] By suppressing all external influences outside a narrow bandwidth near the excitation frequency, this approach enables high resolution and low noise measurements; although frequency dependent thruster characterizations are inherently limited to slow variations, see Section III. This dynamic detection method also obviates the need for extensive design and characterization of a damping mechanism often necessary for a steady state low thrust measurement by either (direct[19,23] or impingement[27]-based) approach.

A description of the thrust-stand is provided in Section II. Thrust measurement up to 50 μN with a noise-floor lower than 10 nN has been demonstrated in Section III from a sub-sonic cold-nitrogen source operating in atmospheric condition. The total impingement force on the plate has been compared with a direct measurement of thrust on the capillary and the results agree within 10%. The noise-floor of the thrust measurements taken inside a vacuum chamber is lower than 10 nN between 5 Hz $\leq f_{\text{ref}} \leq$ 15 Hz and thrust measurements up to 3 μN have been demonstrated in Section IV for an electrospray device emitting high velocity charged ions and droplets inside a vacuum chamber using an electrostatic gate electrode to periodically (10 Hz) modulate the thrust.

II. DESCRIPTION OF THE THRUST-STAND

The thrust-stand operates by measuring the impingement force of the jet emitted by the thruster on a sensing plate. This technique allows the sensing element to be very low-mass and hence to have a natural frequency well above building vibrations. To measure the force on the sensing plate, we use a MEMS-based capacitive force probe, against which the plate is pushed by the thruster beam. A schematic of the thrust-stand and its operating principle are shown in Figures 1(a) and 1(b).

The force sensor, mounted on a translation stage is first brought in contact with the suspended plate, producing a force F_{OFF} on the sensor. The microthruster, aligned on the central axis of the plate, is then fired at the other side of the plate, which intercepts all the emitted particles. This produces an additional force F on the plate, related to the thrust Th from the microthruster, which is what we seek to determine. It can be shown that[32]

$$F = \left(1 + \frac{k_{\text{p}}}{k_{\text{f}}}\right)(F_{\text{meas}} - F_{\text{OFF}}), \tag{1}$$

where F_{meas} is the force sensor reading, k_{p} is the spring constant of the beams of the suspended plate for displacement of the plate normal to its plane (z-direction), and k_{f} is the spring constant of the force sensor. The impingement force, F, can be determined by measuring the increase in force sensor output ($F_{\text{meas}} - F_{\text{OFF}}$) when the microthruster is operated. The thrust on the microthruster, Th, is related to the impingement force, F, by the generalized relation[25]

$$Th = \frac{1}{(1+K)}F, \tag{2}$$

where $0 \leq K \leq 1$ is an effective coefficient of restitution given by the ratio of the linear momentum of the particles normal to the plane of the plate after and before impinging the plate. K depends on the type of impact of the emitted particles with the plate and is discussed in the context of sub-sonic cold-nitrogen and electrospray emission in Sections III and IV, respectively.

To decrease noise and to minimize the effect of possible mechanical drift on force measurements, a lock-in measurement is performed with the impingement force, F applied periodically on the plate (either by pulsing the thruster or by interrupting the impinging plume periodically) at a frequency f_{ref} in square-wave shape. The force sensor output thus alternates periodically between F_{OFF} and F_{meas}. The r.m.s. value,

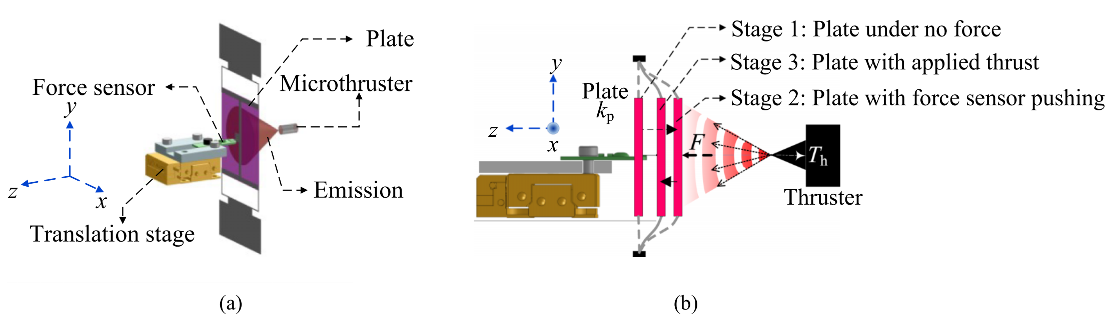

FIG. 1. (a) Schematic of key elements of the thrust-stand. The emitted beam from the microthruster is intercepted by a sensing plate, which pushes against the force sensor, whose output is related to the thrust as described in the text. (b) Operating stages of the thrust-stand. The force sensor is first brought in contact with the plate using the translation stage. Then, the thruster is turned on, and the complete emitted beam from the microthruster is intercepted by the plate. The thrust is delivered in pulses to enable a homodyne measurement for lower noise. The force sensor measures the impingement force on the plate.

R_{out}, of the first harmonic of the periodic force sensor output voltage is directly measured with a lock-in amplifier (Model SR850 from SRS) operating at the same reference frequency f_{ref} and the impingement force, F, is obtained as

$$F = \frac{\pi}{\sqrt{2}} \times \left(1 + \frac{k_p}{k_f}\right) S_F R_{out}, \tag{3}$$

where S_F is the sensitivity of the force sensor, i.e., force per unit change of output voltage and the factor $\pi/\sqrt{2}$ is the ratio of the peak-to-peak value of a square wave signal to the r.m.s. value of its first harmonic. The impingement force can be measured with a resolution F_{res} and up to a range F_{max} given by

$$F_{res} = \left(1 + \frac{k_p}{k_f}\right) F_{\Delta}, \tag{4}$$

$$F_{max} = \left(1 + \frac{k_p}{k_f}\right) (F_{range} - F_{OFF}), \tag{5}$$

where F_{Δ} and F_{range} are the resolution and maximum measurable force of the force sensor. The force sensing element in the thrust-stand is a model FT-S100 force sensor from FemtoTools, which can measure up to $F_{range} = 100\ \mu$N force with a resolution $F_{\Delta} = 5$ nN having spring constant $k_f = 50$ N/m and sensitivity typically $S_F = 50\ \mu$N/V but individually calibrated for each device. To measure higher thrusts (10's of mN) other force sensors, such as FT-S1000, FT-S10000, or FT-S10000 with higher ranges from the same manufacturer can simply replace the FT-S100 force sensor. The force sensor is mounted on a vacuum compatible piezo-motor driven translation stage (Model AG-LS25-V6 from Newport, 50 nm minimum incremental motion).

The sensing plate consists of a central square region to intercept the beam, and four springs, one at each corner. The plate is designed to meet the following criteria:[32]

1. To ensure $F_{res} \leq 10$ nN, one requires $k_p \leq k_f$. Since $k_f = 50$ N/m, the suspended plate is designed with $k_p \leq 50$ N/m.
2. The plate's natural frequency f_p is chosen to be between 50 Hz and 100 Hz. Building vibrations occur mostly at sub-Hz frequencies. In a vacuum chamber, the vibrations from the pumps can be at several 100's of Hz. For a homodyne measurement, f_{ref} should be chosen where the electrical noise and facility vibrations are minimal. Our design targets a natural frequency far from both low-frequency and high frequency bands of facility vibration. f_{ref} is then chosen to be a few Hz, which is well below f_p and yet clear of the low and high frequency vibration bands.
3. The plate's spring constant, k_p, should be independent of both the location where the particle plume impinges on the plate and of the diameter of the impinging beam. To ensure this, the particle intercepting region of the suspended plate, shown in Figure 2(a), is designed to be at least 100 times stiffer than the spring region of spring constant $k_p \leq 50$ N/m, such that the particle intercepting region remains flat when the beams deflect normal to the plane of the plate under applied force, with less than 1% error associated with the spot-size and location on the particle intercepting region.
4. The size of the particle-intercepting region should be large enough to capture the entire plume emitted over a wide emission angle. For example, the emission half-angle of electrospray devices can be as high as 40° (Ref. 33). To ensure that the present design is compatible with such sources, the particle intercepting area is therefore chosen to be 45 mm × 45 mm such that it can capture all emitted particles from a 3 cm distance, with an emission half-angle as high as 40°.
5. The particle capturing area has to be electrically conductive for compatibility with charged beam sources (such as electrospray microthrusters).

To reduce the mass of the sensing plate enough to keep $f_p \geq 50$ Hz, the sensing region consists of an aluminum frame covered by aluminized mylar. Aluminum is chosen for its low Young's modulus E and relatively high E/ρ for manufacturing the springs and plate frame, where ρ is the density. For simplicity of fabrication, all beams and frame elements were laser cut from 130 μm thick Al sheet. To increase the second moment of inertia, and hence the stiffness, of the arms of the frame in the particle intercepting region, the arms are plastically deformed out of plane of the plate using a punch in the form of a semi-circular indent about the axis of the arms as shown in Figure 2(b). The inner diameter of the indent is set to ten times the thickness of the frame so that it can be bent as desired using a punch. To cover the entire particle intercepting area, a 2 μm thick pre-stretched mylar membrane metallized with 20 nm of aluminum is attached on the frame using 25 μm thick ARclear® 8154 adhesive as shown schematically in Figure 2(b). The metallization side of the membrane faces towards the microthruster (to collect a charged beam). In order to achieve electrical contact between the metallization side of the membrane and the aluminum frame, a 2 mm diameter circular aperture in the membrane, close to the center of the frame, is filled with EPOTEK® H20S two-part conductive epoxy. The structure is modeled using finite element methods within the COMSOL multiphysics software package and the dimensions, marked in Figures 2(a) and 2(b), have been optimized for the desired range of spring constant and natural frequency. From a few possible sets of dimensions that can provide the desired spring constant and natural frequency, the chosen dimensions are $L_s = 10$ mm, $L_t = 6$ mm, $b = b_t = b_i = 0.5$ mm, thickness $h = 130\ \mu$m and $d_i = 1.3$ mm; the simulated spring constant is $k_p = 50.2$ N/m (slightly above k_f) and natural frequency $f_p = 81.8$ Hz. The stiffness of the particle intercepting region is computed to be nearly 124 times higher than that of the spring region.

Figures 2(c) and 2(d) show an image of a manufactured plate and a microscopic image of the semi-circular indent on one of the frame-arms, respectively. The natural frequencies of the manufactured plates are measured by analyzing their step responses with a laser displacement sensor (Keyence model LK-H022). The spring constants are measured with a load cell (Futek model LRF-400) and a mechanical stage. The spring constant and natural frequency of plate, used for thrust measurement from the cold-nitrogen ejecting capillary, are 48.2 N/m and 58.2 Hz, respectively, with less than 1% uncertainty.[32]

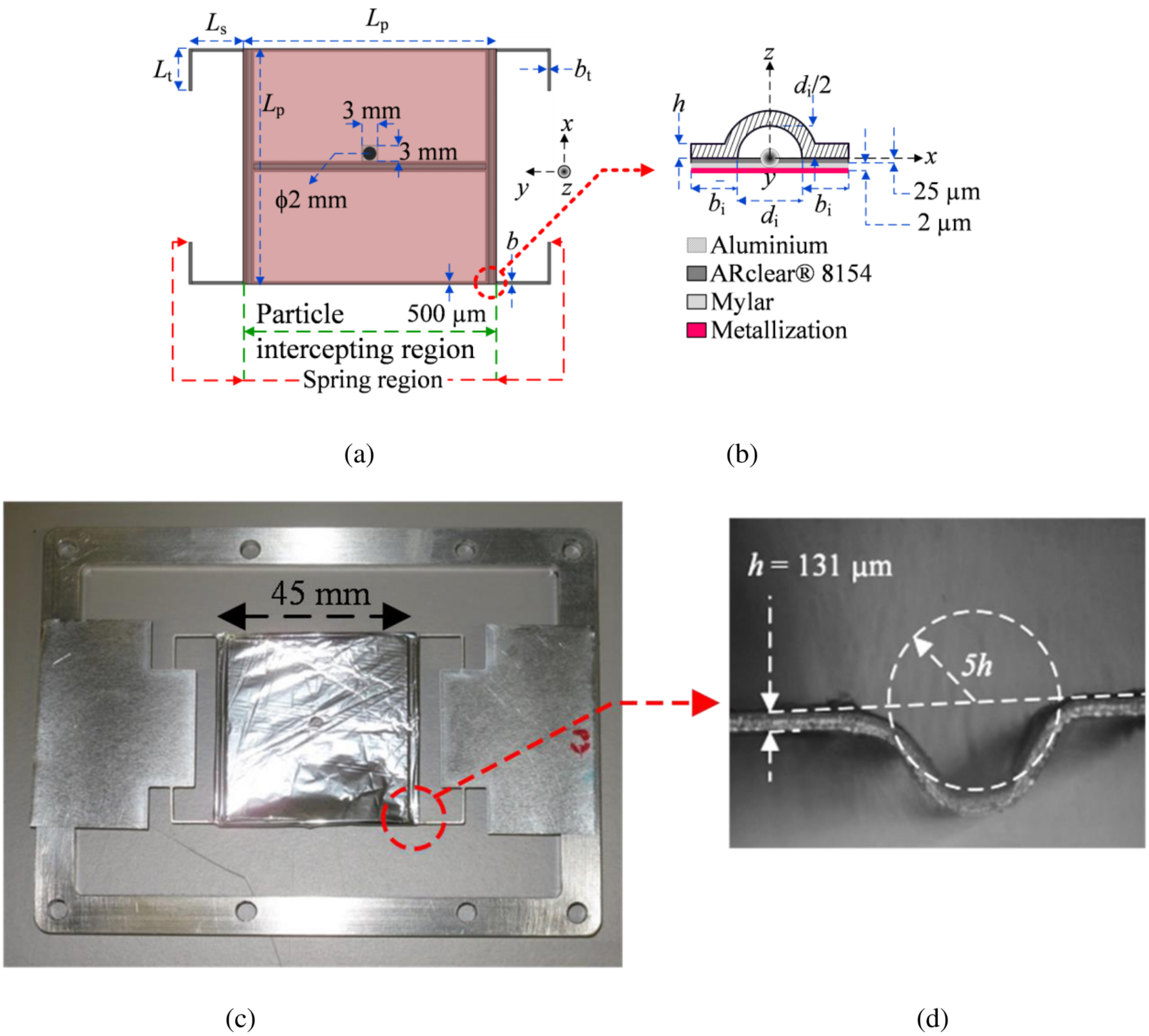

FIG. 2. (a) Schematic of the particle intercepting plate. The particle intercepting region is a frame covered with metallized mylar membrane using ARclear 8154 adhesive for attachment. (b) Cross section schematic of a frame arm showing the out-of-plane indent, stamped before laser-cutting beams, to increase stiffness. (c) Image of a manufactured plate. (d) Microscopic image of the semi-circular indent of the frames. The thickness of the plate is $h = 130$ μm and the semi-circular indent is intended to have an inner diameter $10h$. The supporting springs are not indented to maintain low spring stiffness.

These metrics are, approximately, in agreement with requirements 1 and 2 stated above; a spring constant equal to 50 N/m and a natural frequency between 50 and 100 Hz. While the spring constant agrees with that simulated to within 4%, the discrepancy in natural frequency is indicative of further development required to improve the simulation fidelity when evolving the design.

III. ATMOSPHERIC CHARACTERIZATION WITH A COLD-NITROGEN EMITTING CAPILLARY

The purpose of the atmospheric characterization setup is to experimentally verify the noise-floor, resolution, and measurement accuracy within a 50 μN thrust range. The thrust-stand with a cold-nitrogen thruster is mounted inside a plastic box on a vibration isolation table. A silica capillary of inner diameter 150 μm and length 18 mm at a distance 8 mm from the plate is used to emit a sub-sonic stream of nitrogen. A complete schematic of the lock-in thrust measurement scheme is given in Figure 3(a) with a picture of the setup in Figure 3(b). A three-way electrically controllable pressure switch (SMC model V100) is used to periodically pulse the inlet pressure between the ambient pressure, P_0 and P_{in}, set by a pressure controller (Fluigent model MFCS-8C, better than 1 mbar resolution) having a 1 mm diameter soft-tube outlet. A transistor-transistor logic (TTL) signal at the reference frequency, f_{ref}, internally generated from the lock-in amplifier (SRS model SR850) is used to control the switch. Since the hydraulic impedance of the capillary is much larger than the hydraulic impedance of the soft tube, the Mach number at the inlet of the capillary is $M_{inlet} \ll 1$ and the flow of the nitrogen gas through the capillary can be assumed nearly incompressible and viscosity dominated.[34] Under these conditions, it can be shown that the thrust on the capillary is proportional to $(\Delta P)^2$, where $\Delta P = (P_{in} - P_0)$ is the pressure difference across the capillary. Experimental evidence on thrust from sub-sonic cold-gas[25–27] suggests that $K \approx 0$. Under these conditions, the measured impingement force on the plate and thrust on the capillary can be written as[32]

$$F = Th = \alpha(\Delta P)^2, \tag{6}$$

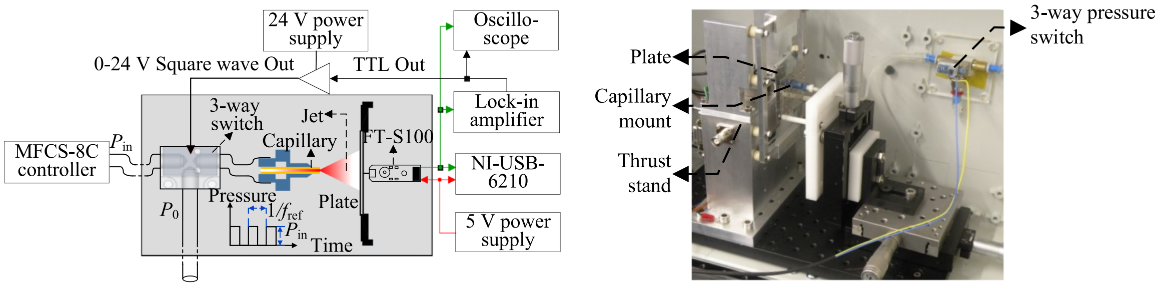

(a) (b)

FIG. 3. (a) Schematic of the atmospheric characterization setup of the thrust-stand using a nitrogen gas emitting capillary. The pressure at the inlet of the capillary is pulsed using a three-way pressure switch. The shaded region is inside a plastic box to stop air currents. (b) Image of the atmospheric characterization setup for the thrust-stand. The entire setup is inside a plastic box and on a vibration isolation table.

where α is a constant that depends on the inner dimensions of the capillary and on the viscosity of cold nitrogen gas. The output of the force sensor is monitored with the lock-in amplifier, operating at f_{ref} and with time constant $T_c = 3$ s and 24 dB/octave roll-off for its phase sensitive detector (PSD). The output of the force sensor is also observed directly with an oscilloscope (Lecroy wavesurfer 424), triggered at the rising edge of the TTL reference signal. The thrust noise-floor at different frequencies is determined by averaging the lock-in amplifier output with $\Delta P = 0$ mbar for 100 s for f_{ref} values between 1 Hz and 10 Hz. One obtains a noise-floor less than 10 nN between 3 Hz $\leq f_{ref} \leq$ 10 Hz (equivalent to less than 60 nN/$\sqrt{\text{Hz}}$ noise spectral density at $T_c = 3$ s with 24 dB/octave roll-off) with vibration isolation enabled as well as disabled, indicating that a minimum thrust of around 10 nN can be potentially detected with the thrust-stand. There is a few nN offset partly contributed by the random facility vibrations in the pass-band of the PSD and partly due to coupling of vibrations of the pressure-switch operating at f_{ref}. The low noise levels achieved through this technique and these lock-in settings come at the expense of an ability to observe thruster stability over short periods. At the configured 3 s time constant, changes in the thruster output, for example, through fluctuations in the feed pressure, manifest in the output subjected to a settling time of ∼12–15 s. Variations in thruster output at higher rates will be suppressed.

For thrust measurement, ΔP is increased in steps, and at each step, the lock-in amplifier output is monitored for 100 s. In Figure 4(a), the pulsating force output traces, recorded with the oscilloscope and averaged over 32 traces, are shown at f_{ref} = 1 Hz and f_{ref} = 4 Hz for the same pressure difference of 400 mbar across the capillary. High frequency fluctuations are superimposed on the otherwise square-wave pulse shapes of the force sensor output. However, the lock-in amplifier selects the first harmonic of the signal at f_{ref} and its time constant and sharp roll-off decouple these high frequency fluctuations, drift, and sub-Hz facility vibrations in the output, providing high signal to noise ratio, and hence reliable thrust measurement at lower thrust levels than possible using only the oscilloscope.

The Fourier transform of the traces shown in Figure 4(a) at two different f_{ref} are shown in Figure 4(b). The amplitude of the first odd harmonic, which is directly measured by the lock-in amplifier, decreases as the reference frequency f_{ref} is increased from 1 Hz to 4 Hz. This is due to finite slope at the rising and falling edge of the square-wave force sensor outputs, arising from the response time, typically a few ms, of the under-damped plate. This finite slope distorts the square-wave shape of the pulses, more so for higher reference frequencies, leading to a reduction in the first harmonic amplitude at f_{ref}, and evolution of even harmonics at $2f_{ref}$ which are absent in a perfect square wave signal. Consequently, the conversion of the lock-in amplifier output, R_{out}, to the peak-to-peak force, F, using Eq. (3) needs to be corrected to take into account the reduction of the amplitude of the first harmonic. In Figure 4(c), a comparison is made between the average lock-in amplifier output and that obtained from the Fourier transform of the

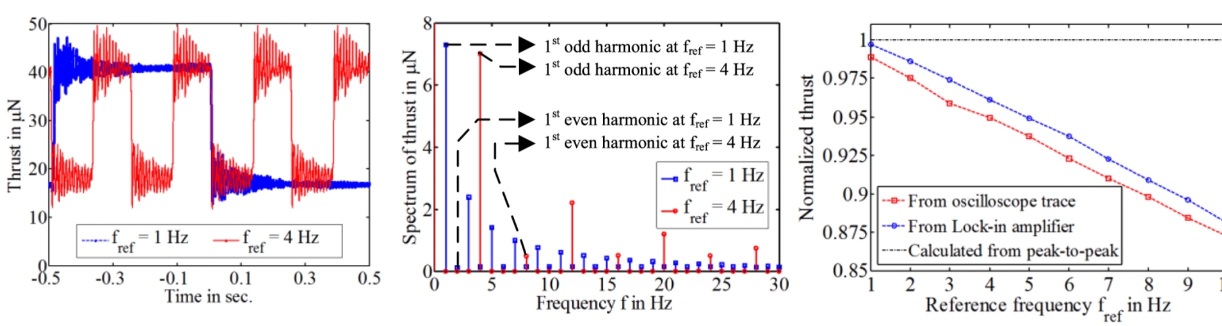

(a) (b) (c)

FIG. 4. Thrust measurements using a cold-gas thruster at 400 mbar. (a) Oscilloscope traces of the raw force sensor output operating at f_{ref} = 1 Hz and 4 Hz. (b) Fourier transform of the oscilloscope traces at f_{ref} = 1 Hz and 4 Hz showing the dependence of the first harmonic amplitude on f_{ref}. (c) Comparison of the thrust measured from (i) the first harmonic of the oscilloscope trace, (ii) the lock-in amplifier, and (iii) the peak-to-peak amplitude measurement of the oscilloscope traces.

oscilloscope traces as f_{ref} is increased from 1 Hz to 10 Hz. Both these outputs are converted to the corresponding peak-to-peak value and normalized by the peak-to-peak force measured from the oscilloscope traces. Both outputs are smaller than the peak-to-peak signal and decrease with increasing f_{ref}. The typically 1%–2% difference between the first harmonics from oscilloscope readings and the lock-in amplifier reading is due to the vertical gain inaccuracy of the oscilloscope. At lower f_{ref} the difference between actual peak-to-peak and that obtained from the first harmonic measurement decreases; however, the noise-floor increases above 10 nN at below 3 Hz. Therefore, $f_{\mathrm{ref}} = 4$ Hz is selected for thrust measurement, which leads to a multiplication factor of 1.05 to be incorporated in Eq. (3).

In Figure 5(a), average thrust output measured by the lock-in amplifier averaged over 100 s is plotted as a function of the pressure difference ΔP, varied 0 mbar to 400 mbar in 10 mbar steps (blue line labeled FT-S100). The standard deviation of the measured thrust at each pressure difference is shown as error-bars and also in the inset. The measured thrust follows a parabolic variation with pressure as expected from Eq. (6). The standard deviation of the measured thrust is below 10 nN for up to around 30 μN thrust levels and typically between 10 nN and 20 nN above 30 μN thrust levels.

To verify that the total thrust is indeed the thrust measured on the sensing plate, we compare the thrust measured with the thrust-stand with that measured directly on the capillary. To do this, one and three identical capillaries are mounted on a load cell (Futek model LRF-400) and the thrust per capillary is directly measured. The load cell has a 100 mN force range and can only resolve forces to a few μN resolution. The average and standard deviation of three successive measurements of thrust per capillary from one and three capillaries with the load cell are also plotted on Figure 5(a) (red and black lines). It can be seen that the directly measured thrust on the capillary with the load cell follows the thrust measured with the thrust-stand using the sensing plate very closely, indicating validity of $F \approx Th$, but with around 10% uncertainty due to relatively large standard deviation of the load cell measurements.

In order to estimate the minimum resolvable thrust from the thrust-stand, measurements are repeated from pressure difference of 0 mbar to 40 mbar in steps of 1 mbar with all other the settings identical to that described above. In Figure 5(b), the average and standard deviation of 100 s of thrust measurement at each pressure difference are plotted. A minimum thrust well-below 10 nN can be detected and thrust differences less than 10 nN can be resolved in this sub-μN thrust range.

Cold-gas thrust measurements were repeated at varied distances between the capillary and the plate from 8 mm to 24 mm. The measured thrust changed by less than 1% despite increase of the spot-size by a factor of three on the plate. This is similar to the observations by Wu *et al.*[26] and indicates that the impingement force measurement is independent of the spot-size of the particle plume on the plate. A 0.2% uncertainty between repeated measurements with the same plate and around 2% uncertainty using different manufactured plates has been observed. By laterally offsetting the capillary from the central axis of the plates by up to 10 mm, a plate dependent 3%–7% maximum reduction in measured force is observed, reflecting the most significant source of uncertainty of the measured impingement force.

IV. THRUST MEASUREMENT FROM AN ELECTROSPRAY DEVICE

We operated our thrust-stand in a vacuum chamber to measure the thrust from an electrospray device, emitting a beam composed principally of ions. The ionic-liquid electrospray device used for thrust measurement is a porous borosilicate emitter strip array, emitting from ionic liquid EMI-BF_4 and capable of up to 10's of μA beam current, details of which can be found elsewhere.[6] For electrospray devices, indirect thrust measurement by time-of-flight mass spectrometry (ToF-MS) has been the most widely used method, but it requires a good knowledge of the beam composition.[6–9] Direct measurement of thrust has also been performed for some electrospray propulsion devices.[6,8,19] If an electrospray emitter emits a current I of particles with uniform kinetic energy qV_{em}, the normal thrust on the device can be written as[6]

$$Th = \beta_0 \gamma_0 I \sqrt{\frac{2m_0 V_{\mathrm{em}}}{q}}, \tag{7}$$

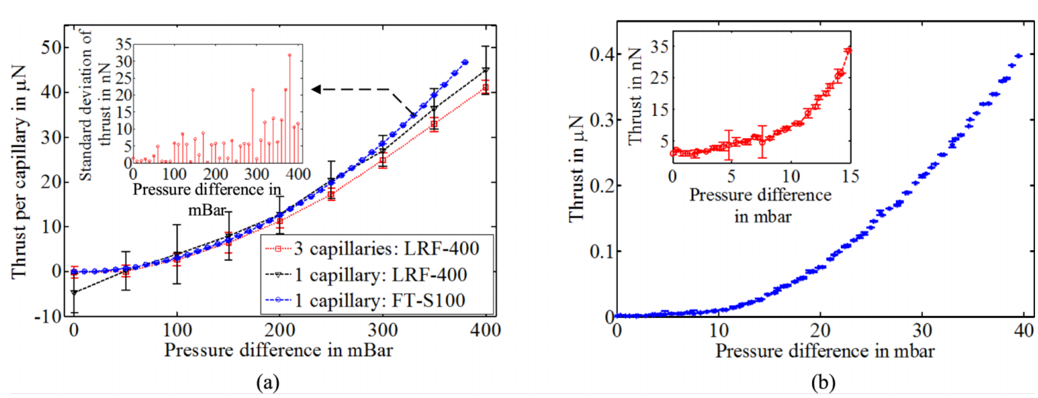

FIG. 5. (a) Measured thrust per capillary vs. applied nitrogen pressure difference. Blue data with error bars smaller than data points form the lock-in output of the force sensor reading the force on the sensing plate (i.e., thrust-stand). Inset: standard deviation of the thrust measurement with the thrust-stand. Red and black data points are direct thrust measurements taken with a load cell, showing much higher noise but confirming agreement between direct thrust and thrust intercepted by sensing plate. (b) Measured thrust from thrust-stand vs. applied pressure difference up to 40 mbar to determine detectable thrust and resolution. Thrusts values well below 10 nN can be resolved with the thrust-stand.

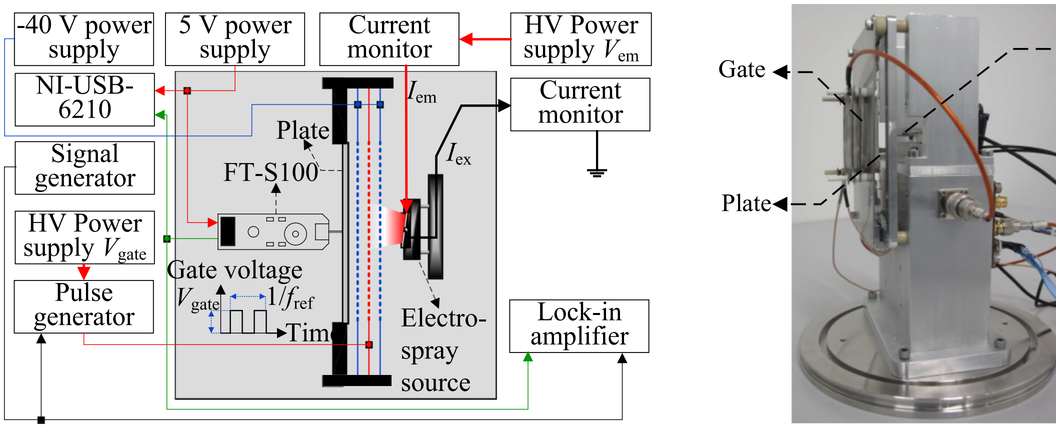

(a) (b)

FIG. 6. (a) Schematic of the thrust-stand for thrust measurement from an electrospray device. An electrostatic gate is used for pulse the thrust (the source emits continuously, but the beam is periodically electrostatically deflected). The shaded region is inside the vacuum chamber. (b) Image of the thrust-stand with the gate electrode assembly mounted on a flange ready to install inside the vacuum chamber.

where m_0 and q are mass and charge of a monomer emitted from the ionic liquid. γ_0 is a factor that takes into account the emission of different charge species together and is obtained from ToF traces of the emission.[6] β_0 is a factor that corrects for the angular spread of the emission into the thrust normal to the axis of emission and is obtained from measurement of current density as a function of angle from the axis of emission.[6] The values of γ_0 and β_0 are measured before the thrust measurements and are, $\gamma_0 = (1.45 \pm 0.03)$ and (1.63 ± 0.07), and $\beta_0 = (0.93 \pm 0.01)$ and (0.93 ± 0.01) in positive and negative polarities of emission, respectively.[32]

The thrust-stand is mounted on a flange of a vacuum chamber and installed inside the vacuum chamber with the sensing plate placed 28 mm away from the emitter. A schematic of the setup is shown in Figure 6(a) and a picture in Figure 6(b). For the homodyne detection, we interrupt the impinging beam using an electrostatic gate. The gate consists of a stainless steel three-electrode grid assembly, the middle grid periodically set to the gate voltage and the other two fixed at −40 V to reduce secondary electron emission from the plate under charge bombardment. This assembly is placed between the sensing plate and the electrospray emitter. Each electrode has a 50 mm diameter aperture with stainless steel grid of 81% optical transparency. The emitted beam current, I, is obtained by subtracting the extractor current, I_{ex}, between the extractor electrode and ground (i.e., beam intercepted by the extractor electrode) from the total emitter current, I_{em} supplied by the high voltage emitter power supply. The gate signal, pulsated at the reference frequency, f_{ref}, between 0 V and V_{gate} = 3000 V or −3000 V depending on emission polarity, is generated using a high voltage pulse generator (DEI model PVX-4140) controlled by a signal generator, and the same control signal is used as reference input for the lock-in amplifier. The noise-floor of the thrust-stand output is typically around 10 nN for f_{ref} between 5 Hz and 15 Hz with T_c = 1 s and 24 dB/octave roll-off (equivalent to noise spectral density less than 40 nN/$\sqrt{\text{Hz}}$). Again, controlled changes in the thruster output will manifest slowly, at a rise time greater than 4 s for these lock-in settings. Thrust measurement has been performed at f_{ref} = 10 Hz. The vibrations of the turbomolecular pump and primary pump do not excite the plate at this frequency.

In Figures 7(a) and 7(b), the thrust measured by the thrust-stand and that obtained indirectly from Eq. (7) by measuring I have been plotted for positive and negative polarities of emission. Here, a multiplication factor of $1/(0.81)^3 = 1.88$ is

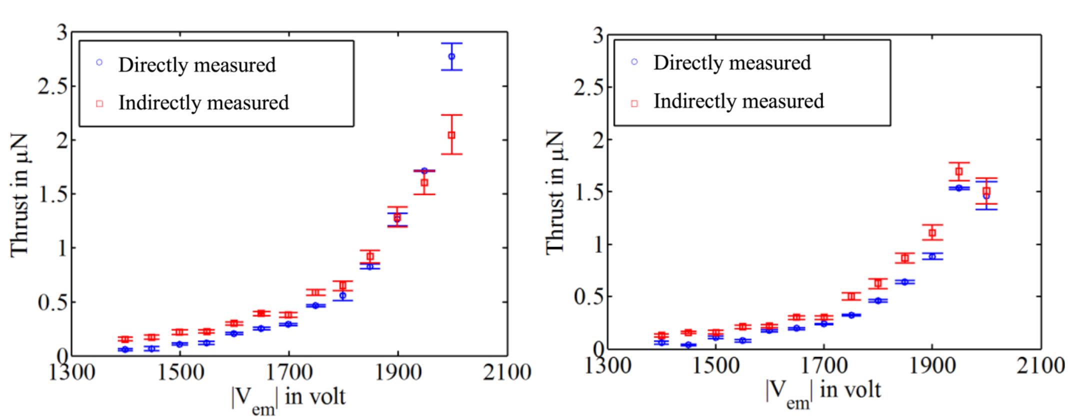

(a) (b)

FIG. 7. Measured thrust from the porous borosilicate electrospray emitter (colloid thruster). Plot of thrust measured at f_{ref} = 10 Hz using the thrust-stand and indirectly computed thrust from beam diagnostics for (a) positive and (b) negative polarities of emission.

included in Eq. (2) to take into account the transparency of the three-electrode assembly between the emitter and the plate. The error-bars on the measured thrust represent the standard deviation of thrust measurements for 38 s and the error-bars on the indirectly calculated thrust using Eq. (7) represents the propagated standard deviations of γ_0, β_0, and I. The average thrust values are very close to each other, typically 50 nN–150 nN less than that obtained from ToF measurement up to the maximum measured thrust. This discrepancy could be partly due to uncertainty in the values of γ_0, β_0, and K used to calculate thrust along with deficits in the kinetic energy of emitted charged particles from qV_{em}. Furthermore, the measured thrust being lower than that calculated is consistent with some population of emitted particles becoming neutral prior to the electrostatic gate, a phenomenon known to occur through fragmentation of solvated ions in flight.[35] The minimum thrust measured with the thrust-stand is below 50 nN. The use of a sensing plate, and the low noise levels and vibration immunity it affords, is thus validated by the agreement between the thrust measurements using two different techniques.

The thrust measurement apparatus lifetime is limited using electrospray thrusters as the energetic charged beam sputters the thin aluminum from the mylar membrane. This indicates a non-zero value of K in Eq. (4). Sputtering yield simulation[36] suggest that for $|V_{em}|$ between 1 kV and 2 kV, the value of K can be between 0.04 and 0.07[32] in positive and negative polarities of emission, which has been incorporated in calculating thrust Th from directly measured F in Figures 7(a) and 7(b); however, more work needs to be done for accurate estimation of K for electrospray thrust measurement and to make a more robust plate less susceptible to sputtering (for example, using graphite layer instead of aluminum metallization[29]) so that higher thrusts from electrospray devices and other electric propulsion devices can also be measured for a long measurement duration without completely eroding the aluminum metallization layer.

V. CONCLUSION

In this article, a nano-Newton thrust-stand has been reported that can measure thrust with 10 nN resolution by measuring the impingement force of the beam emitted from the microthruster using a plate to intercept the beam. By physically isolating the thruster, this thrust-stand alleviates challenges associated with measuring low thrust-to-mass devices and reduces disturbances due to physical connections to the thruster. The particle intercepting plate has a natural frequency over 50 Hz and a homodyne thrust measurement technique has been demonstrated to measure thrust from a cold-gas ejecting capillary and from an electrospray emitter, demonstrating that thrust measurement is possible for different types of microthrusters. The reference frequency and time constant for measurement are chosen to ensure a noise-floor well-below 10 nN, making thrust measurement as low as 10 nN possible. Measurement from a cold-gas ejecting capillary at 4 Hz has demonstrated that thrust up to 30 μN with a resolution better than 10 nN, and thrust above 30 μN with resolution better than 20 nN can be measured. The impingement force measurement has been compared with direct measurement of thrust on the capillary and the results agree to within their respective uncertainties. Thrust measurement up to 3 μN has been performed from an electrospray device with minimum detectable thrust of less than 50 nN. This compact thrust-stand, thus, provides state-of-the-art resolution and noise-floor. The methodology could be scaled up to measure thrust in the 10's of mN ranges, simply by replacing the FT-S100 force sensor with force sensors with higher range.

Limitations and necessary improvements to the thrust-stand have been discussed. Thrust accuracy is limited in part by a required correlation between thrust on the microthruster and impingement force on the plate. Furthermore, although the implemented homodyne detection scheme enabled a high-resolution and low noise measurement, the slow settling time of the lock-in amplifier at the chosen settings limits measurement of thrust variations to sub-Hz ranges. The measurement speed can be improved by reducing the time constant of the lock-in amplifier, but at the expense of a higher noise-floor. When applied specifically to ion thrusters, two limitations are identified. First, electrostatic gating is not effective on neutral particles. Hence, a reduced accuracy is anticipated when measuring thruster plumes which include significant populations of high speed neutral particles. Finally, ablation of the sub-μm thick aluminum coating on the impingement plate presently limits the lifetime of the apparatus.

ACKNOWLEDGMENTS

The authors are grateful to Dr. Caglar Ataman for important discussions. This work was partially supported by the Swiss National Science Foundation under Grant No. 200021_146365, and European Space Agency Network/Partnering Initiative No. 4000109063/13/NL/PA.

[1]J. Mueller, R. Hofer, and J. Ziemer, *Survey of Propulsion Technologies Applicable to CubeSats* (Jet Propulsion Laboratory, Colorado, USA, 2010).
[2]D. Spence, E. Ehrbar, N. Rosenblad, N. Demmons, T. Roy, S. Hoffman, D. Williams, V. Hruby, and C. Tocci, "Electrospray propulsion systems for small satellites," in Proceedings of the 27th Small Satellite Conference, Paper SSC13-VII-5, 2013.
[3]U. Kvell, M. Puusepp, F. Kaminski, J.-E. Past, K. Palmer, T.-A. Gronland, and M. Noorma, Proc. Est. Acad. Sci. **63**(2S), 279–285 (2014).
[4]F. Ceccanti, L. Paita, U. Cesari, M. De Tata, N. Giusti, P. Balducci, M. Del Pistoia, D. Nicolini, and L. Di Napoli, in 31st International Electric Propulsion Conference, Paper IEPC-2009-170, Ann Arbor, Michigan, USA, 20–24 September 2009.
[5]S. Dandavino, C. Ataman, C. N. Ryan, S. Chakraborty, D. Courtney, J. P. W. Stark, and H. Shea, J. Micromech. Microeng. **24**, 075011 (2014).
[6]D. G. Courtney, S. Dandavino, and H. Shea, "Comparing Direct and Indirect Thrust Measurements from Passively Fed and Highly Ionic Electrospray Thrusters," J. Propul. Power (in press), preprint available at http://infoscience.epfl.ch/record/212755.
[7]K. W. Stark and A. Sherman, "Research and development in needle and slit colloid thrusters," NASA TN D-5305, Goddard Space Flight Centre, Washington, DC, USA, 1970.
[8]R. S. Legge, Jr. and P. C. Lozano, J. Propul. Power **27**(2), 485–495 (2011).
[9]G. Lenguito and A. Gomez, J. Appl. Phys. **114**, 154901 (2013).
[10]J. K. Ziemer, T. M. Randolph, G. W. Franklin, V. Hruby, D. Spence, N. Demmons, T. Roy, E. Ehrbar, J. Zwahlen, R. Martin, and W. Connolly, in Proceedings of the IEEE Aerospace Conference, Big Sky, MT, USA, 6-13 March 2010.
[11]L. F. Velásquez-García, A. I. Akinwande, and M. Martínez–Sánchez, J. Microelectromech. Syst. **15**(5), 1272–1280 (2006).
[12]R. H. Lee, A. M. Bauer, M. D. Killingsworth, T. C. Lilly, J. A. Duncan, and A. D. Ketsdever, AIAA Paper 2007-5185, 2007.

[13] See http://www busek.com/cubesatprop__e main.htm for information about different types of micro-propulsion devices.

[14] S. Rocca, C. Menon, and D. Nicolini, Meas. Sci. Technol. **17**, 711–718 (2006).

[15] E. Canuto and A. Rolino, ISA Trans. **43**, 169–187 (2004).

[16] J. P. Lake, G. Cavallaro, G. Spanjers, P. B. Adkison, and M. J. Dulligan, "Resonant operation of a micro-Newton thrust stand," AFRL-PR-ED-TP-2002–308, Air Force Research Laboratory, Edwards AFB, CA, USA, 2003.

[17] J. K. Zeimer, in Proceedings of the 27th International Electric Propulsion Conference, Paper IEPC-01–238, Pasadena, CA, USA, 15-19 October 2001.

[18] D. Packan, J. Jarrige, P. Thobois, C. Blanchard, and P.-Q. Elias, in Proceedings of the 33rd International Electric Propulsion Conference, Paper IEPC-2013-418, Washington, DC, USA, 6-10 October 2013.

[19] M. Gamero-Castaño, Rev. Sci. Instrum. **74**(10), 4509–4514 (2003).

[20] A. J. Jamison, A. D. Ketsdever, and E. P. Muntz, Rev. Sci. Instrum. **73**(10), 3629–3637 (2002).

[21] C. Phipps, J. Luke, T. Lippert, M. Hauer, and A. Wokaun, J. Propul. Power **20**(6), 1000–1011 (2004).

[22] Y. X. Yang, L. C. Tu, S. Q. Yang, and J. Luo, Rev. Sci. Instrum. **83**, 015105 (2012).

[23] J. Soni and S. Roy, Rev. Sci. Instrum. **84**, 095103 (2013).

[24] J. P. Luna, C. H. Edwards, J. G. del Amo, and B. Hughes, in Proceedings of the 32nd International Electric Propulsion Conference, Paper IEPC-2011-011, Weisbaden, Germany, 11-15 September 2011.

[25] S. Hoffman and J. J. Janos, "Force due to air and helium jets impinging normal to a flat plate for near-vacuum and sea-level ambient pressures," NASA TN D-7002, NASA Langley Research Centre, Washington, DC, USA, 1971.

[26] C. K. Wu, H. X. Wang, X. Meng, and W. X. Pan, Acta Mech. Sin. **27**(2), 152–163 (2011).

[27] A. N. Grubišić and S. B. Gabriel, Meas. Sci. Technol. **21**, 105101 (2010).

[28] B.-x. Du, Y. Zhao, W. Yao, and X.-q. Chen, J. Meas. Sci. Instrum. **4**(2), 103–110 (2013).

[29] B. W. Longmier, B. M. Reid, A. D. Gallimore, F. R. Chang-Diaz, J. P. Squire, T. W. Glover, G. Chavers, and E. A. Bering, J. Propul. Power **25**(3), 746–752 (2009).

[30] M. D. West, C. Charles, and R. W. Boswell, Rev. Sci. Instrum. **80**, 053509 (2009).

[31] Y. Takao, K. Eriguchi, and K. Ono, J. Appl. Phys. **101**, 123307 (2007).

[32] S. Chakraborty, "An electrostatic ion-guide and a high-resolution thrust-stand for characterization of micro-propulsion devices," Ph.D. dissertation (EPFL, Switzerland, 2015).

[33] S. Chakraborty, C. Ataman, S. Dandavino, and H. Shea, in Proceedings of PowerMEMS, Atlanta, USA, 2-5 December 2012, pp. 528–531.

[34] P. Hill and C. Peterson, *Mechanics and Thermodynamics of Propulsion*, 2nd ed. (Addison-Wesley, 1992), p. 70.

[35] P. C. Lozano, "Energy properties of an EMI-Im ionic liquid ion source," J. Phys. D: Appl. Phys. **39**(1), 126–134 (2006).

[36] See http://www.srim.org for information about SRIM simulator.